Blind 5G NR LEO Initial Access Receiver

Chen Jaminon-De Roeck, Timothy Otim, Giuseppe Santaromita, and Domenico Giustiniano
IMDEA Networks Institute
Madrid, Spain
{chen.jaminon-deroeck, timothy.otim, giuseppe.santaromita, domenico.giustiniano}@networks.imdea.org

***Abstract*—LEO satellite links pose severe challenges for 5G Non-Terrestrial Network (NTN) initial access due to large carrier frequency offsets, rapidly varying Doppler, and low SNR, making fully blind operation essential in cold-start scenarios. Using a real 5G NTN LEO over-the-air testbed emulation, we show that Doppler compensation accuracy directly governs user equipment (UE) connection outcomes, with residual errors below 3 kHz required for reliable synchronization and attachment. We then present a fully blind, feedforward receiver that computes bounded reliability scores at each processing stage and uses them for hypothesis gating, burst selection, conservative log-likelihood ratio (LLR)-domain combining, weighting, and final lock decisions. The design includes a conservative, reliability-aware multi-Synchronization Signal Block (SSB) Physical Broadcast Channel (PBCH) soft-combining stage that only supplements single-SSB channel quality assessment. Deterministic results from 3GPP-compliant simulations demonstrate robust blind synchronization under ±100 kHz frequency offsets and successful PBCH decoding at low signal-to-noise ratios in urban line-of-sight (LOS) and non-line-of-sight (NLOS) conditions. The simulation code used is publicly available.**

I. Introduction

WITH ongoing 3GPP standardization 5G Non-Terrestrial Network (NTN) support, Low Earth Orbit (LEO) systems are a promising solution for extending wireless connectivity to regions where terrestrial infrastructure is limited or unavailable.

However, current 3GPP NTN standards typically rely on auxiliary state information such as Global Navigation Satellite System (GNSS) positioning, satellite ephemeris, and SIB19 (System Information Block 19) parameters to precompensate for propagation delays and Doppler effects [1]–[3]. Consequently, initial access is tightly coupled to GNSS availability; when this signal is obstructed, network attachment often fails [4], [5].

LEO mobility further complicates synchronization due to the extremely high relative velocities involved exceeding 7.5 km/s. This produces carrier frequency offsets on the order of tens of kilohertz at carrier frequencies around 2 GHz, along with Doppler rates of several hundred hertz per second during a single pass [5]. These impairments introduce time-varying phase rotations across the synchronization window, complicating timing acquisition and frequency estimation. Insufficient compensation leads to inter-carrier interference (ICI) and loss of Orthogonal Frequency-Division Multiplexing (OFDM) orthogonality [6]. The problem is further exacerbated at the low SNRs typical of LEO downlink budgets in Urban NLOS conditions, where receivers may converge to apparently valid but physically inconsistent synchronization states. *Consequently, achieving reliable fully blind initial access in 5G NTN remains a critical and unresolved challenge.*

Existing solutions exhibit several limitations. In 3GPP NTN specifications, satellite-side Doppler pre-compensation is applied based on predicted geometry and characterized through ppm-equivalent residual offsets that depend on beam footprint and cell location. This approach implicitly assumes the availability of coarse spatial information, which may not be accessible during blind access, leaving the receiver responsible for handling the remaining Doppler. While pre-compensation can reduce residual offsets to below approximately 4.7 kHz at a carrier frequency of 2.5 GHz [2], it relies on infrastructure-side knowledge of beam or cell parameters that may be impractical in unassisted scenarios. Moreover, reliance on satellite-side Doppler pre-compensation may complicate practical deployment, as it increases dependence on accurate geometry prediction and tighter network-side coordination.

Conversely, without pre-compensation, offsets can reach tens of kilohertz (e.g., ∼50 kHz at 2.5 GHz), preventing reliable synchronization lock. Academic approaches have also often depended on geometric priors [7]–[9] or iterative estimators [10].

Moreover, many previous studies rely primarily on analytical models or link-level simulations, as experimental studies using real 5G waveforms and full protocol stacks remain limited. A few studies within European Space Agency (ESA) research initiatives, such as 5G-GOA [11] and 5G-LEO [12] have emulated 5G NTN scenarios using software-defined radios and 5G NR software platforms like OpenAirInterface [13] to examine Doppler effects on NR waveforms. However, these efforts are dependent on simulated NTN channels and primarily rely on emulated or controlled environments, thereby overlooking system-level dynamics.

In this work, we address the blind NTN initial access through the following contributions:

- Using a real 5G NTN LEO over-the-air emulation platform, we demonstrate that residual Doppler accuracy directly governs user equipment (UE) attachment behavior. Residual CFO must be constrained to a few kHz to avoid repeated Random Access retransmissions and attachment failure.
- Motivated by this observation, we design a fully

blind, reliability-guided 5G NR NTN receiver. The feedforward pipeline exploits SSB structure without GNSS, ephemeris, timing advance, or prior Doppler information, while bounded reliability metrics guide hypothesis selection and allow robust decoding under severe Doppler and low SNR.

- We develop a 3GPP-compliant simulation framework to evaluate blind initial access under realistic NTN conditions, including Doppler offsets exceeding 50 kHz, Doppler rates of several hundred hertz per second, and SNRs down to -40 dB in Urban LOS and NLOS channels.
- Finally, we introduce a multi-SSB PBCH soft-combining strategy. Log-likelihood ratio (LLR)-domain combining uses reliability-aware weighting based on blind noise estimation and burst-level LLR quality indicators. The weights are bounded and normalized to enforce stable aggregation and prevent artificially inflated decoding performance.

The focus of this work is the blind initial-access interval before NTN assistance becomes available. Consequently, the evaluation targets Doppler and SNR conditions representative of this short cold-start segment of a LEO pass. The code used for the implementation and simulations in this work is open source[1].

II. State of the Art and Limitations

Prior works have investigated Doppler estimation and compensation for LEO satellite communication systems. Geometry-based approaches derive Doppler evolution from satellite motion models assuming constant angular velocity and known orbital trajectories [7]–[9]. While analytically tractable, these methods require prior information such as UE position and satellite ephemeris, and often assume static or slowly moving terminals conditions that may not hold during cold-start or GNSS-denied operation.

Approximate signal models have also been proposed. For example, [14] models Doppler using a second-order Taylor expansion. Although computationally attractive, such truncations introduce modeling error under the nonlinear Doppler evolution characteristic of LEO systems, particularly at large offsets and high Doppler rates.

Blind signal-domain methods avoid geometric knowledge by estimating Doppler directly from received samples [10], [15], [16]. However, many techniques rely on iterative refinement and extended observation windows, increasing computational burden and limiting suitability for short listening times or constrained UE hardware. Cyclic-prefix (CP)-based estimators are widely used due to their simplicity, but their inherent ambiguity range is limited to approximately $\pm\frac{1}{2}\Delta f$ subcarrier spacing (about ± 15 kHz for 30 kHz numerology), which is insufficient to resolve the tens-of-kilohertz offsets typical of LEO NTN [17].

[1]https://github.com/chen-jaminonderoe/Blind_5G_NR_LEO_Initial_Access_Receiver.git

More generally, prior work proceeds with refinement and decoding even when intermediate timing or frequency evidence are weak. Under severe mobility and low SNR this can increase the incidence of false synchronization rather than controlled acquisition failure. Finally, the majority of prior studies are validated primarily through analytical modeling or link-level simulation. While valuable for theoretical insight, such evaluations do not fully capture receiver behavior. In real implementations, acquisition decisions depend on implementation specific aspects such as estimator interaction, buffering, decoding confidence propagation, and finite listening-time constraints. As a result, the system-level impact of large Doppler impairments on 5G NTN initial access remains insufficiently understood.

In contrast, the proposed receiver does not rely on geometric priors, iterative feedback refinement, or external positioning assistance. Instead, it follows a strictly feedforward blind synchronization chain in which each stage computes a bounded reliability score used for gating, hypothesis selection, and burst combining. This reliability-guided orchestration across PSS (Primary Synchronization Signal), SSS (Secondary Synchronization Signal), DMRS (demodulation reference signal), and PBCH stages distinguishes the proposed solution from prior estimators.

III. UE Attachment Under Residual Doppler: 5G NTN Emulation

To validate the above theoretical tolerance limits under realistic constraints, we developed a 5G NTN emulation platform using the OpenAirInterface (OAI) stack. The setup comprises next-generation NodeB (gNB) and UE nodes implemented on Ettus Research N310 SDRs, driven by Intel Core i7-8700K workstations via 10 GbE interfaces to sustain real-time 5G NR sampling rates. Over-the-air transmission is enabled by 5 dBi omnidirectional antennas in a controlled laboratory environment.

Satellite Doppler is emulated at complex baseband by applying a programmable phase rotation to the transmitted samples $x(n)$:

$$x'(n) = x(n)\, e^{\frac{j2\pi f_D(t_n)}{f_s}} \tag{1}$$

where $x(n)$ is the original baseband sequence, F_s the sampling frequency, and $f_D(t_n)$ the Doppler shift at time t_n. This approach enables precise and repeatable injection of large frequency offsets representative of LEO NTN conditions while preserving the 5G NR waveform structure. A fixed Doppler shift of 50 kHz comparable to maximum LEO Doppler at 2.5 GHz carrier frequency was injected at the gNB [5], [7]. By systematically varying the residual compensation applied at the UE, the testbed evaluates the impact of Doppler magnitude and mismatch on synchronization stability and higher layer procedures.

Figure 1 shows the UE connection state as a function of residual Doppler error. When compensation is accurate (within a few kilohertz), full attachment succeeds. With moderate mismatch, initial synchronization is achieved but the procedure stalls ("Attach and stop"). Larger residual

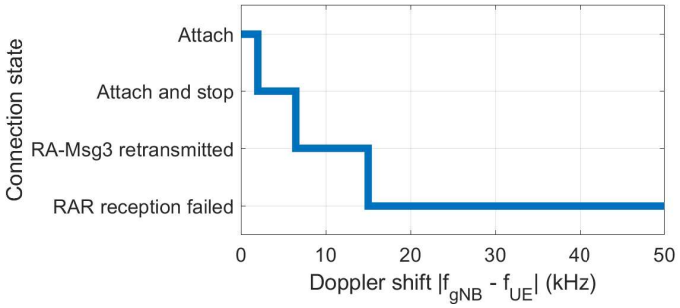

Fig. 1. Illustration of the UE (receiver) connection state as a function of the compensated Doppler shift induced by the motion of a LEO satellite during a real 5G-NTN emulation.

error leads to repeated Random Access Message 3 (RA-Msg3) retransmissions despite Physical Random Access Channel (PRACH) detection. Under severe mismatch, the Random Access Response (RAR) cannot be decoded. These results demonstrate that *reliable 5G NTN operation requires residual Doppler errors within a few kHz, motivating blind acquisition mechanisms* that do not rely on prior positional or assistance information.

IV. System and Channel Model

A. SS/PBCH Structure

We follow 3GPP TS 38.211 [18] and consider the Case B SS/PBCH configuration with numerology $\mu = 1$ (30 kHz subcarrier spacing, FR1). Each SSB occupies $K_{\mathrm{SSB}} = 240$ subcarriers over four OFDM symbols. The PSS and SSS are mapped to the central 127 subcarriers, while the remaining resource elements carry PBCH data and its associated DMRS.

B. Channel Model

The channel combines standardized multipath propagation statistics from 3GPP TR 38.901 [19] with deterministic large-scale LEO Doppler dynamics following TR 38.811 [20].

1) Multipath and Small-Scale Fading: Multipath propagation follows tapped-delay line (TDL) models. Urban NLOS uses the TDL-A profile (Rayleigh fading), while Urban LOS uses TDL-C (Rician fading). Tap delays τ_l and average powers follow the Annex-B parameterization.

Each tap undergoes independent small-scale fading generated using a Jakes-like Sum-of-Sinusoids (SoS) process [21]. LOS taps follow a Rician distribution with scenario-dependent K-factor, while NLOS taps are Rayleigh distributed. The local Doppler spread produced by this SoS process models terminal motion and scatterer dynamics and remains distinct from the deterministic large-scale LEO Doppler drift.

The resulting time-varying channel impulse response is

$$h(\tau, t) = \sum_{l=0}^{L-1} \alpha_l(t)\, \delta(\tau - \tau_l), \tag{2}$$

where $\alpha_l(t)$ are the time-varying complex tap coefficients.

2) Large-Scale LEO Doppler: The large-scale Doppler regime corresponds to a representative circular LEO pass at an altitude of approximately 600 km [2], [20]. Over the short blind-access interval, the nonlinear orbital Doppler evolution is accurately approximated by a first-order model with constant initial offset and Doppler rate:

$$f_D(t) = f_{\mathrm{CFO}} + \dot{f}_D\, t, \tag{3}$$

where f_{CFO} is the initial carrier offset at receiver and $\dot{f}_D$ is the local Doppler rate.

Equivalently, the received phase evolution is

$$\phi(t) = 2\pi \left(f_{\mathrm{CFO}}\, t + \tfrac{1}{2} \dot{f}_D\, t^2 \right). \tag{4}$$

The selected operating point represents a worst-case high-Doppler regime near low-to-mid elevation, where the absolute Doppler shift reaches 40–50 kHz at $f_c = 2$ GHz [5], [7] and the Doppler rate remains in the few-hundred-hertz-per-second range. The deterministic Doppler drift is applied uniformly across all multi-path taps, while the small-scale Doppler spread remains independently captured by the fading process.

V. Proposed Blind Receiver Architecture

We propose a fully blind, reliability-guided receiver for 5G NR NTN initial access. The architecture operates as a strictly feedforward processing chain in which all stages execute deterministically. Each stage produces an estimate together with an associated reliability metric used for downstream hypothesis selection, gating, and, where applicable, weighting.

Figure 2 illustrates the high-level processing flow. Synchronization proceeds through staged refinement: PSS-based coarse estimation, multi-SSB candidate localization, anchor selection, fractional timing correction, blind DMRS hypothesis testing, residual CFO estimation, and PBCH demodulation. The final lock decision is governed by the PBCH CRC outcome, while LLR reliability is used to quantify decoding confidence.

When multiple repetitions of the same SSB index are detected, reliability-weighted multi-SSB LLR combining is performed. The combining weights are bounded and normalized to ensure stable aggregation and to limit the impact of unreliable bursts.

A. Stage 1: Coarse PSS-Based Synchronization and Doppler Search

The receiver performs a two-stage discrete CFO grid search jointly with PSS hypothesis testing to handle the large Doppler offsets typical of NTN scenarios and find the appropriate PSS sequence.

The first stage evaluates a coarse CFO sweep together with the three 3GPP-compliant PSS sequences indexed by $N_{\mathrm{ID}}^{(2)} \in \{0, 1, 2\}$. The coarse search spans the expected NTN Doppler range with safety factor d, here set to $d = 2.4$, using a 5 kHz resolution step:

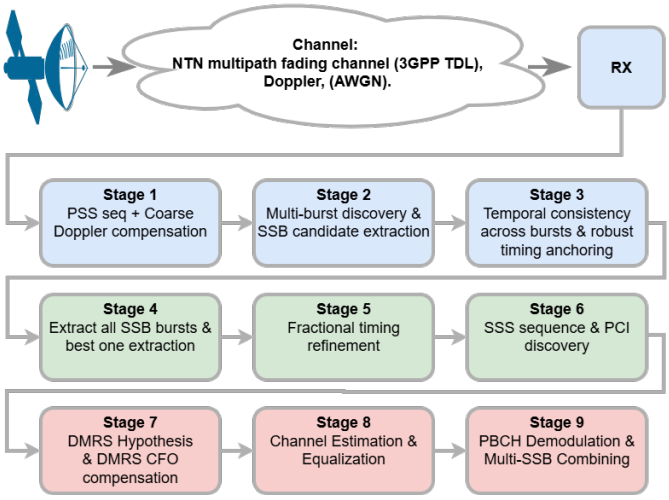

Fig. 2. High-level overview of the proposed blind NTN initial access receiver. All stages execute sequentially without early termination. Reliability measures are propagated forward to weight hypotheses and govern the final decision.

$$f_{\text{coarse}} \in [-d \cdot 50,\ d \cdot 50] = [-120, 120]\ \text{kHz},$$

For each tested coarse CFO–PSS hypothesis, the correlation output is computed as

$$c_{m,r}[n] = \sum_k r[k] e^{-j2\pi f_m k/f_s}\, s^{(r)*}_{\text{PSS}}[k-n]. \tag{5}$$

Here, $r[k]$ denotes the received baseband sample stream, f_m is the tested CFO hypothesis, f_s is the sampling frequency, and $s^{(r)}_{\text{PSS}}[\cdot]$ is the local PSS reference sequence associated with the r-th PSS hypothesis.

A normalized separation metric is then computed as

$$\Gamma(f_m, r) = \frac{\max_n |c_{m,r}[n]|}{\text{median}_n |c_{m,r}[n]| + \varepsilon}, \tag{6}$$

where ε is a small positive constant that ensures numerical stability. The metric emphasizes isolated correlation peaks even under low SNR. The maximizing coarse hypothesis yields the coarse CFO estimate $\hat{f}_{\text{coarse}}$, the detected PSS index $\hat{N}^{(2)}_{\text{ID}}$, and the initial timing estimate $\hat{\tau}_0$. The coarse correction is then immediately applied to the received buffer to remove the dominant Doppler component.

A second refinement stage then searches the residual offset over the uncertainty region defined by the coarse-step resolution. The fine sweep spans one coarse-bin neighborhood with safety margin k, here set to $k = 1.2$, using a 200 Hz resolution step:

$$f_{\text{fine}} \in [-k\Delta f_{\text{coarse}},\ +k\Delta f_{\text{coarse}}],$$

where $\Delta f_{\text{coarse}} = 5$ kHz. This residual search is performed with finer resolution using only the selected PSS sequence. The maximizing residual estimate $\hat{f}_{\text{fine}}$ and refined timing $\hat{\tau}_1$ are retained, and the residual correction is then applied to the signal. The total Stage-1 CFO estimate is therefore

$$\hat{f}_1 = \hat{f}_{\text{coarse}} + \hat{f}_{\text{fine}}.$$

B. Stage 2: Multi-SSB Candidate Localization

After CFO correction, additional SSB occurrences are detected by reapplying PSS correlation using the selected PSS sequence. Local maxima of the correlation magnitude form the candidate timing set

$$\{\hat{\tau}_k\}_{k=1}^{K}. \tag{7}$$

To remove outliers, candidates are filtered using

$$|\hat{\tau}_k - \hat{\tau}_0| \le \Delta_{\max}, \tag{8}$$

C. Stage 3: Timing Anchoring

The detected SSB timing candidates $\{\hat{\tau}_k\}$ are first evaluated for consistency across the observation window, exploiting the periodic transmission of SSB bursts, using

$$\sigma_\tau^2 = \text{Var}\{\hat{\tau}_k\}. \tag{9}$$

A low variance indicates stable repeated detections, while a large variance suggests unreliable localization due to noise or residual Doppler. This statistic is retained as a reliability indicator that contributes to synchronization confidence and subsequent processing.

A single anchor timing reference is then selected from the retained candidates as

$$\hat{\tau}_{\text{ref}} = \hat{\tau}_{k^\star}, \tag{10}$$

where $k^\star$ corresponds to the strongest PSS correlation peak.

D. Stage 4: SSB Extraction and Segmentation

Using the selected anchor SSB, the receiver constructs two aligned waveform views: a local anchor-burst buffer used for fine timing refinement and hypothesis testing, and a full-signal buffer spanning all detected SSB candidates with guard margins for later multi-burst processing.

At this stage, all burst start locations are mapped into a common full-buffer coordinate system. The common timing reference is then defined as

$$\tau_B = (\tau_{\text{int}}, \tau_{\text{frac}}),$$

where τ_{int} is the integer-sample location of the anchor SSB in the full received buffer and τ_{frac} is a fractional correction term initialized to zero. This representation ensures that all subsequent stages operate on a common timing basis.

E. Stage 5: Fractional Timing Refinement

Fractional timing refinement is then performed using the anchor SSB local buffer to update the fractional component of the common timing reference. A raw fractional

estimate δ_{raw} is obtained from the PSS region and evaluated over a small candidate set

$$\delta \in \{\delta_{\text{raw}} + \Delta_i\}.$$

Each candidate is assessed using a blind PSS-based error metric,

$$\hat{\delta} = \arg\min_{\delta} \mathcal{E}(\delta),$$

where δ denotes the tested fractional timing hypothesis and $\mathcal{E}(\delta)$ is an Error Vector Magnitude (EVM)-like proxy evaluated over the anchor SSB using the known PSS sequence after coarse equalization. The fractional timing correction is applied only if it reduces this metric; otherwise, only the integer timing is retained.

F. Stage 6: SSS Detection and Physical Cell Identity (PCI) Resolution

With timing fixed, the receiver detects the SSS in the frequency domain. For each of the 336 valid SSS hypotheses $N_{\text{ID}}^{(1)} \in \{0, \ldots, 335\}$, the correlation metric

$$M\left(N_{\text{ID}}^{(1)}\right) = \left| \sum_{k \in \mathcal{K}_{\text{SSS}}} Y(k,3)\, s_{\text{SSS}}^{*}\left(k; N_{\text{ID}}^{(1)}, \hat{N}_{\text{ID}}^{(2)}\right) \right| \quad (11)$$

is evaluated, where $Y(k,3)$ denotes the received frequency-domain resource element at subcarrier index k on the third OFDM symbol of the SSB, $\mathcal{K}_{\text{SSS}}$ is the set of the 127 SSS subcarrier indices, and $s_{\text{SSS}}(\cdot)$ is the locally generated 3GPP-compliant SSS sequence for the tested hypothesis.

The maximizing index yields $\hat{N}_{\text{ID}}^{(1)}$ and the physical cell identity

$$\hat{N}_{\text{ID}} = 3\hat{N}_{\text{ID}}^{(1)} + \hat{N}_{\text{ID}}^{(2)}. \quad (12)$$

The SSS detection margin is retained as a reliability index for subsequent processing stages.

G. Stage 7: Blind DMRS Hypothesis Resolution and Residual CFO Estimation

In this stage, the receiver performs a blind search over the eight possible SSB index hypotheses

$$\bar{i}_{\text{SSB}} \in \{0, \ldots, 7\}.$$

For each hypothesis of the SSB index $\bar{i}_{\text{SSB}}$, the corresponding PBCH DMRS sequence $X_i(k,2)$ is generated and evaluated using a scalar least-squares fit to the canonical DMRS OFDM symbol. Let $\mathcal{K}_{\text{DMRS}}^{(2)}$ denote the DMRS subcarrier set on the selected symbol. The scalar channel hypothesis is estimated as

$$\hat{H}_i = \frac{1}{|\mathcal{K}_{\text{DMRS}}^{(2)}|} \sum_{k \in \mathcal{K}_{\text{DMRS}}^{(2)}} \frac{Y_{\text{DMRS}}(k,2)}{X_i(k,2)}. \quad (13)$$

The detected SSB index is obtained from the hypothesis minimizing the residual DMRS matching error

$$E(i) = \sum_{k \in \mathcal{K}_{\text{DMRS}}^{(2)}} \left| Y_{\text{DMRS}}(k,2) - \hat{H}_i X_i(k,2) \right|^2. \quad (14)$$

The selected hypothesis then directly yields the half-frame index n_{HF} and PBCH scrambling parameter v.

Residual CFO is estimated from the DMRS phase evolution across OFDM symbols and applied to the full signal buffer when the DMRS reliability metric indicates a stable estimate. OFDM symbols are then re-sliced using the common timing reference.

H. Stage 8: Single-SSB Channel Equalization

Channel equalization is performed on a per-SSB basis using two candidate channel models: a scalar PSS-based estimate and a frequency-selective DMRS-based estimate. For either hypothesis,

$$Y_{\text{eq}}(k,m) = \frac{Y(k,m)}{\hat{H}(k,m)}, \quad (15)$$

where $\hat{H}(k,m)$ denotes either the scalar PSS channel estimate applied uniformly over the full SSB or the interpolated least-squares DMRS channel estimate over the SSB grid. When blind DMRS hypothesis resolution is unavailable or unreliable, the receiver safely falls back to the scalar PSS-based equalizer.

The equalized signal yielding the lower blind, decision-directed EVM over the PBCH resource elements is selected for subsequent demodulation,

$$\text{EVM} = \frac{\mathbb{E}\{|Y_{\text{eq}} - \hat{X}|^2\}}{\mathbb{E}\{|\hat{X}|^2\}}, \quad (16)$$

where $\hat{X}$ denotes the nearest QPSK constellation points obtained from the equalized PBCH symbols.

I. Stage 9: PBCH Demodulation and Multi-SSB Combining

For each detected SSB, PBCH symbols are extracted. A blind thermal-noise variance estimate is first obtained from noise-only resource elements and used for PBCH bit-wise LLR computation from the equalized QPSK symbols of burst b, yielding the per-burst LLR vector $\mathbf{L}_b$.

In parallel, an effective variance σ_b^2 is formed by augmenting the blind noise variance with penalties derived from DMRS phase dispersion and synchronization reliability. This quantity is retained as a burst-reliability indicator for confidence interpretation and combining diagnostics, without directly modifying the PBCH LLR scaling.

When multiple repetitions of the same SSB index are available, the corresponding PBCH LLR vectors are combined before polar decoding as

$$\mathbf{L}_{\text{comb}} = \sum_{b} w_b \mathbf{L}_b,$$

TABLE I. Simulation Parameters

Parameter	Urban NLOS	Urban LOS
3GPP Profile	TDL-A	TDL-C
Area / Visibility	Urban / NLOS	Urban / LOS
RMS Delay Spread	200 ns	5 ns
Small-Scale Fading	Rayleigh ($K = -\infty$)	Rician ($K = 12$ dB)
Local Doppler ($f_{d,\text{small}}$)	250 Hz	150 Hz
SNR	-20 dB	0 dB
Sampling frequency (f_s)	30.72 MHz	
SSB bandwidth (BW)	7.2 MHz	
LEO Dynamics		
Carrier Frequency (f_c)	2.0 GHz	
Nominal Geometric f_{D0}	38.372 kHz (Worst-case)	
Doppler Rate ($\dot{f}$)	300 Hz/s	
Evaluation Sweeps		
CFO Sweep Range	$[-100, +100]$ kHz	
SNR Sweep Range	$[-50, 0]$ dB	
Listening Time (T_{listen})	$[40, 300]$ ms	

where w_b is the bounded reliability weight associated with burst b. The weights are derived from burst-level LLR reliability metrics, then clipped and normalized to prevent dominance by unreliable bursts. The resulting combined LLR vector is passed to the PBCH polar decoder following the 3GPP specification [22]. The CRC outcome and decision margins are then recorded.

VI. Simulation Setup

The proposed receiver is evaluated using a high-fidelity link-level simulation framework implemented in MATLAB. Channel modeling relies on the 5G Toolbox `nrTDLChannel` object to ensure compliance with 3GPP TR 38.901; when unavailable, a SoS implementation is used.

A. Waveform Configuration

The transmitted waveform follows 5G NR FR1 specifications at carrier frequency $f_c = 2.0$ GHz. Case B SSB configuration with 30 kHz subcarrier spacing ($\mu = 1$) is employed, with 20 ms burst periodicity.

B. Channel and Propagation Model

The simulation separates large-scale LEO Doppler dynamics from small-scale multipath fading, consistent with TR 38.811 and TR 38.901. Two 3GPP-compliant propagation scenarios are evaluated: Urban NLOS (TDL-A) and Urban LOS (TDL-C). All scenario-specific parameters (delay spread, K-factor, local Doppler, baseline SNR) are summarized in Table I.

The geometric Doppler component corresponds to a representative LEO orbit with orbital velocity approximately $v \approx 7.5$ km/s. Although the full orbital Doppler evolution is nonlinear over a complete satellite pass, over the short blind initial-access listening interval (40–300 ms) a first-order local approximation remains physically accurate. The channel therefore applies a nominal Doppler offset f_{D0} together with a constant Doppler rate $\dot{f}$:

$$f_D(t) = f_{D0} + \dot{f}\, t.$$

The adopted Doppler rate $\dot{f} = 300$ Hz/s is representative of a local linearized FR1 LEO NTN segment and remains within the worst-case Doppler-rate range reported by 3GPP studies for 600 km non-GEO deployments, which can approach approximately 500 Hz/s at 2 GHz [2], [20]. Over the maximum 300 ms listening interval used, this corresponds to only 90 Hz of additional drift.

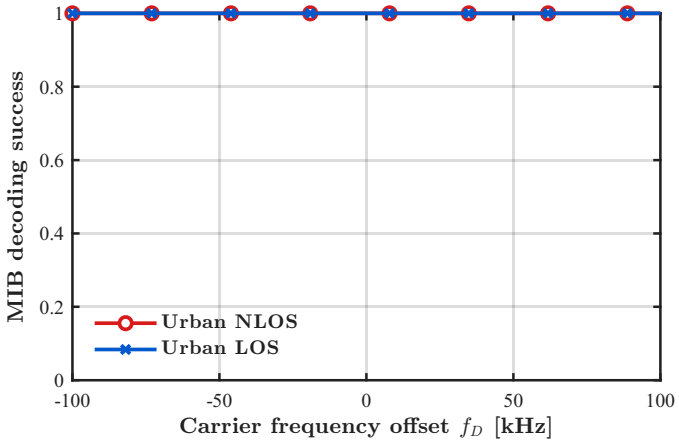

Fig. 3. MIB decoding probability versus carrier frequency offset f_D.

C. Deterministic Sensitivity Analysis

To isolate algorithmic behavior from statistical randomness, simulations operate in deterministic mode, with fixed random number generators for channel realization and thermal noise at each operating point.

VII. Results

This section evaluates the proposed fully blind 5G NR NTN initial-access receiver under cold-start conditions. All results are obtained directly from raw baseband samples, without any prior timing, frequency, or channel knowledge.

Results are reported for two 3GPP-compliant NTN channel models: *Urban NLOS* (TDL-A, Rayleigh) and *Urban LOS* (TDL-C, Rician), with $f_c = 2$ GHz, $\Delta f = 30$ kHz, and deterministic LEO Doppler parameters matching the simulation setup of Section VI.

A. Doppler Robustness and Large-Offset Compensation

Figure 3 shows Master Information Block (MIB) decoding probability versus initial CFO. In this set-up, the worst-case LEO Doppler at 2 GHz is typically 40–50 kHz, while our sweep extends to ± 100 kHz, fully covering the NTN cold-start regime with additional margin.

Reliable decoding is shown to be achieved throughout the full tested range for both LOS and NLOS channels. This indicates that performance is largely insensitive to the initial Doppler magnitude once the correct hypothesis is resolved.

B. Residual Frequency Error

Figure 4 reports the residual frequency error after the final compensation stage. Across the full ± 100 kHz initial offset sweep, the median residual error remains below approximately 300 Hz for both Urban LOS and NLOS.

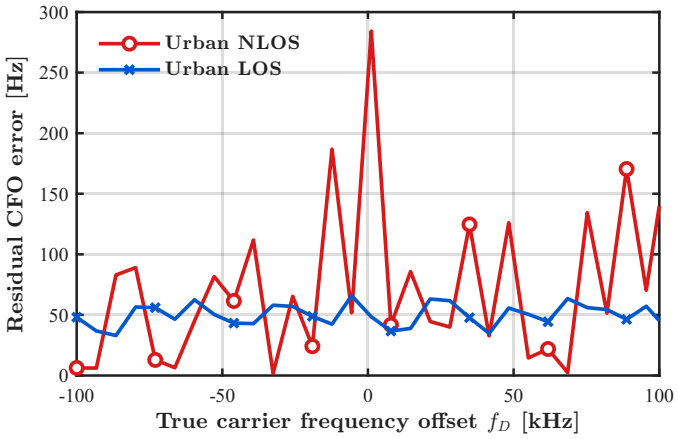

Fig. 4. Median residual CFO estimation error versus initial offset.

The nearly constant error floor across the sweep suggests that the residual error is mainly caused by Doppler variation during the observation window and residual synchronization uncertainty. This behavior is consistent with the Stage-1 coarse/fine search design, which removes most large-offset dependence before DMRS-based refinement.

C. Decodability Versus SNR

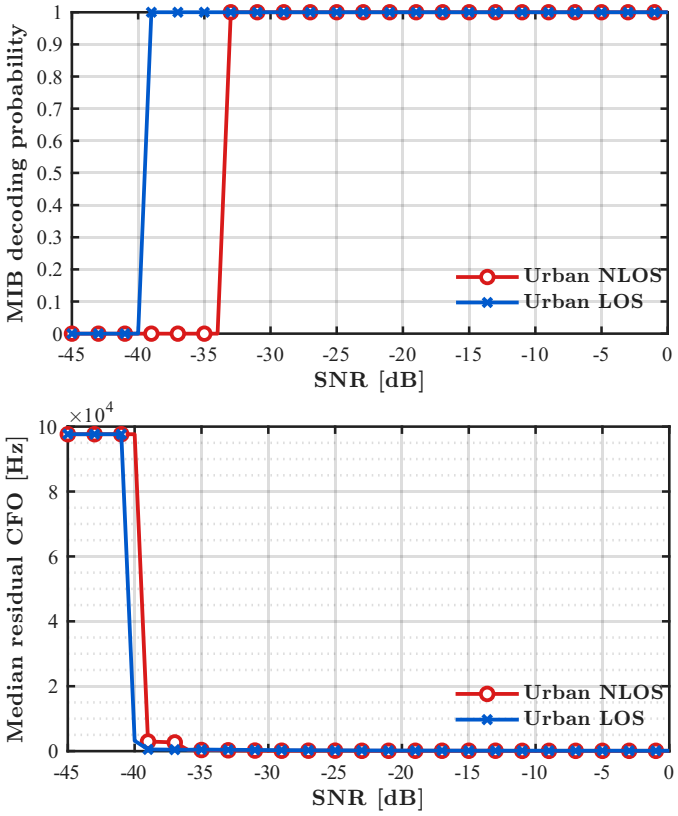

Fig. 5. Performance versus SNR. Top: MIB decoding probability. Bottom: Median residual CFO estimation error.

Figure 5 (top) shows the MIB decoding probability as a function of SNR when multiple occurrences of the same SSB are combined.

A clear threshold appears near $-40\,\mathrm{dB}$ in Urban LOS and $-35\,\mathrm{dB}$ in Urban NLOS. Above this region, residual CFO falls below 1 kHz and PBCH decoding succeeds. Below it, loss of frequency lock leaves residual offsets in the tens of kilohertz, making PBCH decoding impossible. The decoding probability in Fig. 5 is governed by the ability of the receiver to achieve reliable frequency synchronization.

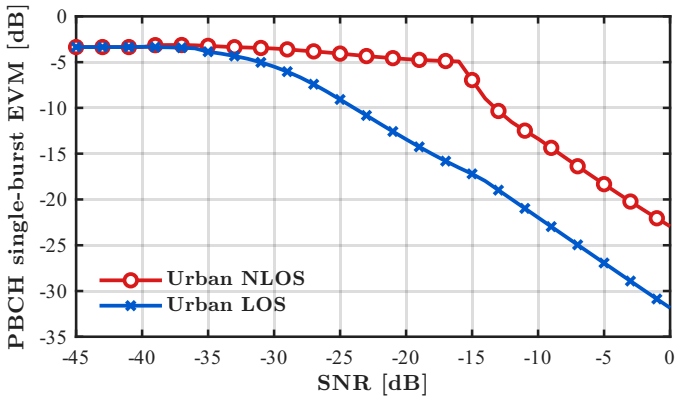

Fig. 6. Single-burst PBCH Error Vector Magnitude (EVM) versus SNR.

D. Single-Burst EVM Behavior

Figure 6 shows the single-burst PBCH EVM versus SNR for Urban LOS and NLOS channels. Under ideal synchronization and additive white Gaussian noise (AWGN), squared EVM is approximated by the inverse of the effective SNR [23]:

$$\mathrm{EVM}^2 \approx \frac{1}{\mathrm{SNR}_{\mathrm{eff}}}, \tag{17}$$

This trend is observed in both channel models once blind synchronization and residual CFO compensation succeed, where distortion is mainly governed by thermal noise and small-scale fading.

At very low SNR, the EVM departs from the AWGN prediction. In this region, residual CFO, timing uncertainty, degraded DMRS-based channel estimation, and occasional synchronization hypothesis errors may jointly contribute to constellation distortion, phase rotation and inter-carrier interference. The curve reflects two regimes: synchronization-limited at very low SNR, and noise-limited after blind frequency lock.

E. Multi-SSB Combining Efficiency

Figure 7 quantifies the effective combining gain obtained from N repetitions of the same SSB. Under stable inter-burst synchronization, LLR-domain soft combining approaches the linear reliability-growth bound

$$G_{\mathrm{coh}} = 20\log_{10} N. \tag{18}$$

By contrast, when repeated bursts provide only weakly correlated soft information, the gain reduces toward the non-coherent reference bound

$$G_{\mathrm{incoh}} = 10\log_{10} N. \tag{19}$$

The effective gain is measured as

$$G_{\text{eff}} = 10\log_{10}\left(\frac{\mathbb{E}\{|L_{\text{comb}}|^2\}}{\mathbb{E}\{|L_{\text{ref}}|^2\}}\right). \tag{20}$$

Here, L_{ref} is the LLR vector from a single SSB burst, while L_{comb} is the reliability-weighted LLR vector after multi-SSB accumulation. The effective LLR-domain combining gain approaches the coherent reference bound in Urban LOS and remains close in Urban NLOS, indicating strong inter-burst soft-information consistency.

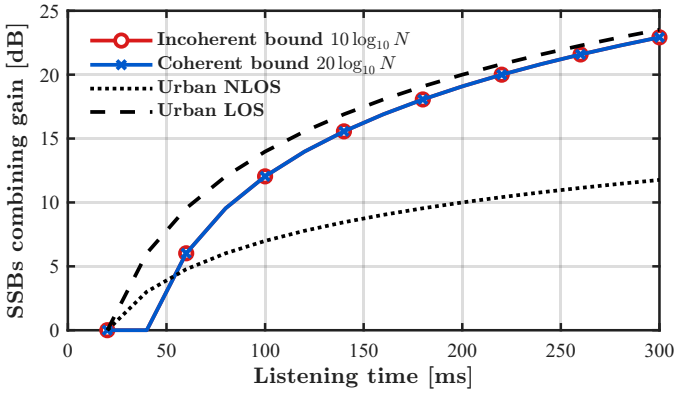

Fig. 7. Effective combining gain versus number of accumulated SSBs.

VIII. Conclusion

The results demonstrate that fully blind 5G NR NTN initial access is feasible under severe LEO Doppler and low-SNR conditions. Offsets up to ±100 kHz are resolved without external assistance, residual CFO is reduced to the sub-kHz range after lock, and bounded multi-SSB combining improves sensitivity while preserving physical realism. These findings establish a practical blind synchronization framework for cold-start NTN access and support future full-stack NTN receiver integration.

Acknowledgments

This work is funded in part by action EUSPA/GRANT/06/2022, that has received funding from the EU/EUSPA. This publication reflects only the author's view and EUSPA is not responsible for any use that may be made of the information it contains. This work is funded in part by project PID2022-136769NB-I00 funded by MCIN/AEI /10.13039/501100011033 / ERDF, UE. Chen-Terry Jaminon-De Roeck's work was additionally supported by MCIN/AEI/10.13039/501100011033 and by the ESF+ under the predoctoral training grant PREP2022-000340.

References

[1] "5G; NR; Radio Resource Control (RRC); Protocol Specification," TS 38.331, Release 19, v19.0.0, 3GPP, 2025.

[2] "Solutions for NR to Support Non-Terrestrial Networks (NTN)," TR 38.821, Release 16, v16.2.0, 3GPP, 2023.

[3] X. Lin *et al.*, "5G from Space: An Overview of 3GPP Non-Terrestrial Networks," *IEEE Communications Standards Magazine*, vol. 5, no. 4, pp. 147–153, Dec. 2021.

[4] M. Giordani and M. Zorzi, "Non-Terrestrial Networks in the 6G Era: Challenges and Opportunities," *IEEE Network*, vol. 35, no. 2, pp. 244–251, 2021.

[5] O. Kodheli *et al.*, "Satellite Communications in the New Space Era: A Survey and Future Challenges," *IEEE Communications Surveys & Tutorials*, vol. 23, no. 1, pp. 70–109, 2021.

[6] P. H. Moose, "A Technique for Orthogonal Frequency Division Multiplexing Frequency Offset Correction," *IEEE Transactions on Communications*, vol. 42, no. 10, pp. 2908–2914, Oct. 1994.

[7] I. Ali, N. Al-Dhahir, and J. E. Hershey, "Doppler Characterization for LEO Satellites," *IEEE Transactions on Communications*, vol. 46, no. 3, pp. 309–313, Mar. 1998.

[8] B.-H. Yeh, J.-M. Wu, and R. Y. Chang, "Efficient Doppler Compensation for LEO Satellite Downlink OFDMA Systems," *IEEE Transactions on Vehicular Technology*, vol. 73, no. 12, pp. 18 863–18 877, Dec. 2024.

[9] J. Lin, Z. Hou, Y. Zhou, L. Tian, and J. Shi, "MAP Estimation Based on Doppler Characterization in Broadband and Mobile LEO Satellite Communications," in *Proc. IEEE 83rd Vehicular Technology Conference (VTC-Spring)*, 2016, pp. 1–5.

[10] J. Wang, C. Jiang, L. Kuang, and B. Yang, "Iterative Doppler Frequency Offset Estimation in Satellite High-Mobility Communications," *IEEE Journal on Selected Areas in Communications*, vol. 38, no. 12, pp. 2875–2888, Dec. 2020.

[11] "5G-GOA Project," https://connectivity.esa.int/archives/projects/5ggoa, European Space Agency, 2026, accessed: 2026-04-15.

[12] "5G-LEO Project," https://connectivity.esa.int/archives/projects/5gleo, European Space Agency, 2026, accessed: 2026-04-15.

[13] "OpenAirInterface," https://openairinterface.org/, OpenAirInterface Software Alliance, 2026, accessed: 2026-04-15.

[14] D. Tian, Y. Zhao, J. Tong, G. Cui, and W. Wang, "Frequency Offset Estimation for 5G-Based LEO Satellite Communication Systems," in *Proc. IEEE/CIC International Conference on Communications in China (ICCC)*, 2019, pp. 647–652.

[15] M. Pan, J. Hu, J. Yuan, J. Liu, and Y. Su, "An Efficient Blind Doppler Shift Estimation and Compensation Method for LEO Satellite Communications," in *Proc. IEEE International Conference on Communication Technology (ICCT)*, 2020, pp. 643–648.

[16] X. Lin *et al.*, "Doppler Shift Estimation in 5G New Radio Non-Terrestrial Networks," in *Proc. IEEE Global Communications Conference (GLOBECOM)*, 2021, pp. 1–6.

[17] J.-J. van de Beek, M. Sandell, and P. O. Börjesson, "ML Estimation of Time and Frequency Offset in OFDM Systems," *IEEE Transactions on Signal Processing*, vol. 45, no. 7, pp. 1800–1805, Jul. 1997.

[18] "NR; Physical Channels and Modulation," TS 38.211, Release 19, v19.2.0, 3GPP, 2026.

[19] "Study on Channel Model for Frequencies From 0.5 to 100 GHz," TR 38.901, Release 18, v18.1.0, 3GPP, 2026.

[20] "Study on New Radio (NR) to Support Non-Terrestrial Networks," TR 38.811, Release 15, v15.4.0, 3GPP, 2020.

[21] Y. R. Zheng and C. Xiao, "Simulation models with correct statistical properties for rayleigh fading channels," *IEEE Transactions on Communications*, vol. 51, no. 6, pp. 920–928, Jun. 2003.

[22] "NR; Multiplexing and Channel Coding," TS 38.212, Release 19, v19.2.0, 3GPP, 2026.

[23] J. G. Proakis and M. Salehi, *Digital Communications*, 5th ed. New York, NY, USA: McGraw-Hill, 2008.